RMetS
Royal Meteorological Society

# The role of evaporating showers in the transfer of sting-jet momentum to the surface

K. A. Browning,[a] D. J. Smart,[b]* M. R. Clark[c] and A. J. Illingworth[d]
[a]*Independent Researcher, Ambleside, UK*
[b]*Department of Earth Sciences, UCL Hazard Centre, UCL, London, UK*
[c]*Observations R&D, Met Office, Exeter, UK*
[d]*Radar Meteorology Group, Department of Meteorology, Reading University, UK*
*Correspondence to: D. J. Smart, UCL Hazard Centre, University College London, 136 Gower St, London, WC1E 6BT, UK.
E-mail: d.smart@ucl.ac.uk



**The most damaging winds in a severe extratropical cyclone often occur just ahead of the evaporating ends of cloud filaments emanating from the so-called cloud head. These winds are associated with low-level jets (LLJs), sometimes occurring just above the boundary layer. The question then arises as to how the high momentum is transferred to the surface. An opportunity to address this question arose when the severe 'St Jude's Day' windstorm travelled across southern England on 28 October 2013. We have carried out a mesoanalysis of a network of 1 min resolution automatic weather stations and high-resolution Doppler radar scans from the sensitive S-band Chilbolton Advanced Meteorological Radar (CAMRa), along with satellite and radar network imagery and numerical weather prediction products. We show that, although the damaging winds occurred in a relatively dry region of the cyclone, there was evidence within the LLJ of abundant precipitation residues from shallow convective clouds that were evaporating in a localized region of descent. We find that pockets of high momentum were transported towards the surface by the few remaining actively precipitating convective clouds within the LLJ and also by precipitation-free convection in the boundary layer that was able to entrain evaporatively cooled air from the LLJ. The boundary-layer convection was organized in along-wind rolls separated by 500 to about 3000 m, the spacing varying according to the vertical extent of the convection. The spacing was greatest where the strongest winds penetrated to the surface. A run with a medium-resolution version of the Weather Research and Forecasting (WRF) model was able to reproduce the properties of the observed LLJ. It confirmed the LLJ to be a sting jet, which descended over the leading edge of a weaker cold-conveyor-belt jet.**

*Key Words:* extratropical cyclone; low-level jets; sting jet; damaging winds; WRF model; Doppler radar

*Received 12 February 2015; Revised 7 May 2015; Accepted 14 May 2015; Published online in Wiley Online Library 02 September 2015*

## 1. Introduction

The concept of the Sting Jet (hereafter SJ) was proposed following a mesoanalysis of the Great Storm of October 1987 (Browning, 2004). SJs occur within some extratropical cyclones and have been identified as a cause of damaging surface winds in several observational studies (Browning, 2004; Parton *et al.*, 2009; Martinez-Alvarado *et al.*, 2014) and in modelling studies (Clark *et al.*, 2005; Martinez-Alvarado *et al.*, 2010, 2014; Smart and Browning, 2014). The kind of cyclone that is prone to generate a SJ conforms to the conceptual model of Shapiro and Keyser (1990), wherein the SJ forms in the frontal-fracture region associated with frontolysis and divergence (Schultz and Sienkiewicz, 2013) at the tip of the bent-back front. SJs are not always responsible for the strongest winds at the surface, but it appears that SJs may be responsible for some of the more extreme events and tend to be difficult to predict.

There is still uncertainty as to the mechanisms responsible for SJs. In addition to the usual ingredients required to produce a rapidly deepening cyclone, the original 2004 study identified conditional symmetric instability (CSI) and cooling by evaporation as possible candidates. Studies by Clark *et al.* (2005), Gray *et al.* (2011) and Martinez-Alvarado *et al.* (2012) have since confirmed that CSI is a common feature of storms producing SJs. Likewise, the same studies have shown that some air-parcel trajectories within SJs do experience significant diabatic cooling. On the other hand, a recent idealized modelling study by Slater *et al.* (2014) suggests that an airstream resembling a SJ can be generated by pressure-gradient forces in the absence of either CSI or evaporational cooling. However, regardless of whether

or not evaporation plays a role in generating a SJ, a case can be made for evaporation being important in helping to bring the momentum associated with a SJ down to the surface.

The difficulty of transferring the momentum of the SJ to the surface has been stressed by Browning (2004), Baker *et al.* (2014) and Smart and Browning (2014). The latter found only very weak downward momentum transport in their idealized simulations. There are two aspects to the problem. First of all, because SJs originate within the frontal zone of the bent-back front, they have a higher wet-bulb potential temperature ($\theta_w$) than, for example, the air in the cold-conveyor-belt jet (CJ) behind the front, which is another low-level jet (LLJ) that can produce damaging surface winds. Second, the air in SJs tends to warm adiabatically while descending from levels in the mid-troposphere. Both these factors increase the static stability at low levels when the SJ reaches down to the top of the boundary layer. Browning (2004) therefore proposed that evaporation within the SJ might be able to cool the air sufficiently to reduce the Richardson number significantly and perhaps even create convective instability, thereby providing a mechanism for bringing down pulses of high momentum all the way to the surface. The fact that the wind damage attributed to SJs occurs downwind of the evaporating tips of cloud filaments at the tip of the cyclone's cloud head provides some support for the plausibility of such a mechanism, but until now there have been no direct observations to confirm it.

The purpose of this article is to present a case study of a storm involving some unique observations that enable us to demonstrate a role for convection and a likely role for evaporation in bringing high momentum from a SJ to the surface in places where damaging winds were encountered. The storm studied was the 'St Jude's Day' storm, which produced swaths of wind damage across southern England on 28 October 2013 before going on to produce even worse damage in continental Europe (where it is also known as 'Windstorm Christian'). Several kinds of observational data are used in the analysis, such as imagery from *Meteosat* and the UK operational weather radar network, but the critical data were obtained from the very sensitive Doppler radar at Chilbolton, Hampshire in southern England, which was operated through the night of 27–28 October by a team led by one of us (AJI). We also make use of a newly automated mesoanalysis procedure (Clark and Parker, 2014) for analyzing the 1 min resolution data from the operational network of automatic weather stations (AWSs), as well as complementary output from a medium-resolution run of the Weather Research and Forecasting (WRF) model. The key observations from the Chilbolton radar were limited to a rather small region in the vicinity of this radar and so we were unable to determine whether the inferred roles for convection and evaporation were applicable to other areas that were also affected by a SJ.

## 2. Data sources and analysis methods

### 2.1. Automatic weather stations

A time-compositing technique was applied to the 1 min resolution AWS data, in which off-analysis-time observations are translated in space using an observed system velocity. Time-compositing has previously been used in a number of studies of convective storms and intense extratropical cyclones (e.g. Fujita 1955, 1958; Browning and Hill, 1984; Browning, 2004). In these studies, time-compositing was generally applied manually. In this case, we apply an automated procedure to the minute resolution AWS data. A detailed description of the procedure is given in Clark and Parker (2014). For each analysis time, compositing was applied over a 40 min period centred on the analysis time. The required system velocity is that of individual trackable surface-wind maxima. The system velocity was obtained using an iterative approach. A 'first guess' velocity was estimated from the movement of the developing low-pressure centre, as shown in Met Office surface analysis charts, available at six-hourly intervals. The time-composited data were interpolated on to a 5 km grid using Delaunay triangulation and analyses of surface parameters were plotted from the gridded datasets. The locations of mesoscale wind maxima were tracked in a sequence of surface wind analyses generated in this way, which provided a refined estimate of the required system velocity. Time-compositing was applied a second time, using the refined motion vector, and the wind maxima in the resulting analyses tracked again. This process was repeated a further two times, after which the difference in the motion vector obtained in successive iterations was negligible.

The underlying assumption of the time-compositing technique is that the system to be analyzed is in a steady state over the compositing period. Therefore, temporal variations in parameter values observed at a single location can be assumed to equate to spatial variations in the direction of system motion. A 40 min period was chosen in this case, because the system evolution was generally small over this period. Furthermore, given the density of observing stations over England, it resulted in good coverage of data points, albeit with a few large gaps. Within the analysis domain, the number of stations recording temperature (dry bulb and dew point), winds and pressure was 123, 71 and 61, respectively. Application of the time-compositing yielded 4920, 2840 and 2440 data points, respectively, for these parameters (Figure 1). Koch and O'Handley (1997) demonstrated that analysis errors associated with the uncertainty in system velocity were only acceptably small when the compositing period is restricted to 55 min or less and the uncertainty in the system velocity is $< 25\%$. The 40 min compositing period used here therefore satisfies Koch and O'Handley's (1997) temporal criterion, whilst the iterative approach to deriving the system motion velocity results in a system velocity uncertainty of $\ll 25\%$.

The minute-resolution AWS data were corrected in a number of ways prior to the application of time-compositing. Firstly, temperature was corrected for altitude assuming a dry adiabatic lapse rate. Secondly, mean wind speed was corrected for site exposure. The correction was obtained by deriving long-term mean wind speeds for each site, during periods of uniform southwesterly winds. Uniform wind events were defined as occasions on which the pressure gradient was uniform across the analysis domain, with negligible curvature of the isobars.

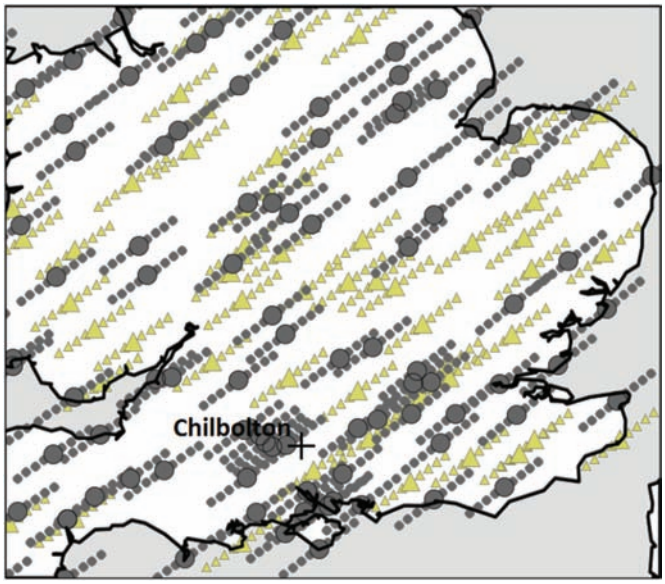


**Figure 1.** Data points obtained by time-compositing of AWS data over a 40 min period, using the observed motion vector of wind maxima over southern England. Circles indicate data points for which wind observations are available. Triangles indicate additional data points for which no wind observations are available (i.e. temperature only or temperature and pressure only). Larger circles and triangles indicate the AWS locations. For clarity, only every fifth data point along the track of data points associated with each AWS is displayed. The location of the Chilbolton radar is marked by the '+'. This figure is available in colour in the online article.

Met Office surface analysis charts were used to identify such events. Under these conditions, the geostrophic wind speed will be invariant over the domain; site-to-site variations in observed mean wind speed should therefore be attributable to variations in site exposure. The analysis was restricted to cases in which the wind direction was between 180° and 270° from north (hereafter all references to direction in degrees are with respect to north), since west to southwesterly winds predominated in the event under study (especially within the mesoscale wind maxima that are of most interest) and the degree of site exposure is likely to show some wind-direction dependence. For each site, the mean wind speed during the identified uniform wind periods was calculated. The overall (i.e. all-site) mean during the same periods was divided by the mean wind speed at an individual site in order to obtain a correction factor for that site. The 1 min values of mean wind speed for the current analysis period were then multiplied by the correction factor obtained for each site in order to provide a 'standard-exposure' mean wind speed at each site.

### 2.2. *The Chilbolton advanced meteorological radar (CAMRa)*

The 10 cm wavelength Doppler radar at Chilbolton is of very high sensitivity and was critical to the detection of the shallow decaying showers that played a key role in the study. Technical details of this radar are described by Goddard *et al.* (1994); however, the important point to note is that not only could it detect the decaying showers out to ranges of over 50 km, but it could also detect boundaries of convection aloft and much of the turbulent boundary layer out to comparable ranges, even where there was no precipitation. Some of the important atmospheric structures in the lower troposphere in the vicinity of the decaying showers were quite small and so another key feature of CAMRa was its 1/4° beam, which leads to a beam width of only 250 m at a range of 50 km. This provides unrivalled spatial resolution when compared with the 1° beam width of most operational and research radars. Fortunately, the path of the strongest surface winds passed directly over Chilbolton, thereby making it easier to sample the region of strong winds at very high resolution. However, the storm was travelling rapidly eastwards and the time when useful data could be obtained was restricted to the short periods just before and after the area of strongest winds passed over Chilbolton.

In order to obtain three-dimensional information, the radar was operated in a sequence of plan position indicator (PPI) and range height indicator (RHI) scans. The excellent sensitivity and resolution of the radar is achieved at the expense of a large (25 m) aerial. Because of the large size of the aerial, the scanning rate that can be achieved is rather slow and therefore, to minimize the time elapsed between successive scanning cycles, the scans were made within restricted sectors. PPI sector scans were made, first to the west of the radar and later to the east, at elevation angles of 0.5°, 1.0° and 1.5°. Interspersed with these were sets of RHI scans at 5° intervals of azimuth. The duration of each combined scanning cycle varied between 7 and 30 min. The interpretation of the CAMRa images involved the diagnosis of patterns of radar reflectivity and Doppler velocity, which shed light on the physical mechanisms that created them. Confidence in the interpretation was gained by analyzing the imagery in the context of the AWS data discussed in section 2.1 and the numerical weather prediction (NWP) data described next.

### 2.3. *NWP model data*

The version of WRF used in this study was the Advanced Research WRF (ARW-WRF) 3.5.1 (Skamarock *et al.*, 2008). A one-way, nested configuration was employed with a large domain ('Domain 1') with 30 km grid spacing on a Lambert conformal grid, covering much of the North Atlantic and northwest Europe region, and a nested 10 km domain ('Domain 2', 301 × 301 horizontal grid points, centred on the UK at 52.5°N, −3°W).

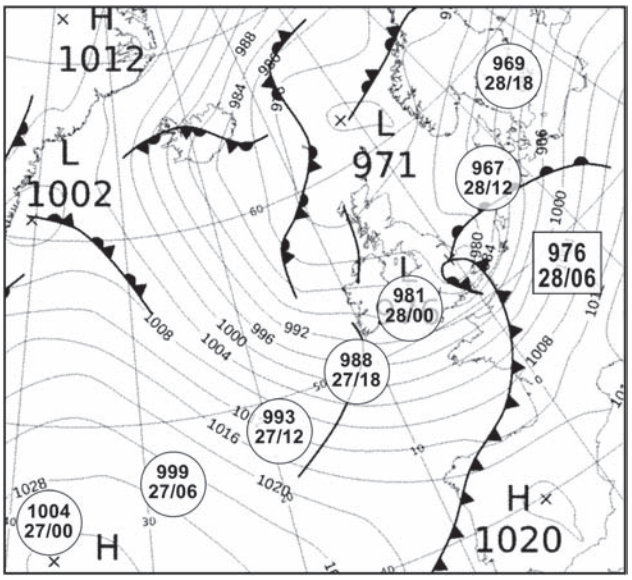


**Figure 2.** Surface analysis at 0600 UTC on 28 October 2013. The central pressure (hPa)/day/time (UTC) of the storm centre is indicated within the square box. The location of the storm centre at other times is indicated within the overlaid circles. (Original chart courtesy and copyright UKMO.)

The vertical grid had 48 levels with a stretching function to give a spacing of 120–240 m in the lower and mid-troposphere, with the lowest, full model level at 24 m above the terrain and the model top at 50 hPa. The initialization data were obtained from the National Centers for Environmental Prediction (NCEP) Global Forecast System (GFS) model final analysis run (GFS-FNL). Additionally, high-resolution (1/12°) NCEP sea-surface temperature (SST) data were incorporated into the initialization data. Both domains were initialized at 0600 UTC on 27 October 2012 and run for 36 h.

Simulations initialized from various GFS operational and final analysis runs from 1–2 days prior to 28 October were found to produce a storm with differing deepening rates and MSLP centres compared with the United Kingdom Meteorological Office (UKMO) analysis of 976 hPa at 0600 UTC on 28 October (see Figure 2), although the track was generally good, thus providing useful guidance for forecasters. The present run was chosen because it verified well in terms of track and also intensity, although it was 2.0–2.5 h fast for much of the storm life cycle.

The physics configuration and vertical discretization of the model are similar to those employed in the simulation of the 3 January 2012 SJ storm analyzed by Smart and Browning (2014). For the simulation reported here, the Kain–Fritsch (KF) cumulus scheme, WRF Single moment Microphysics 6 (WSM6), Dudhia short wave and Rapid Radiative Transfer Model (RRTM) long-wave radiation schemes were employed in both Domain 1 and Domain 2. The Mellor-Yamada-Nakanishi-Niino2 (MYNN2) PBL and surface-layer schemes (Nakanishi and Niino, 2004) incorporating the modifications by Olson* were also used (the apparent problem with diagnosed gusts over land due to the MYNN surface layer scheme in WRF 3.2.1, reported by Smart and Browning (2014), having been corrected in WRF 3.5.1). The reader is referred to Skamarock *et al.* (2008) for further details and references on the WRF parametrization schemes. The horizontal grid spacing of Domain 2, at 10 km, is coarser than that employed by Smart and Browning (2014) for their analysis and was selected in order to reduce the amount of unwanted detail generated by model topography in the present simulation whilst allowing us to diagnose the essential structures due to the system dynamics. As will be shown later (section 6), the simulation reproduces key features of the structure of the LLJs within the storm over southern England, as deduced from observations.

*See the WRF version 3.5.1 source code for documentation and Olson and Brown (2012).

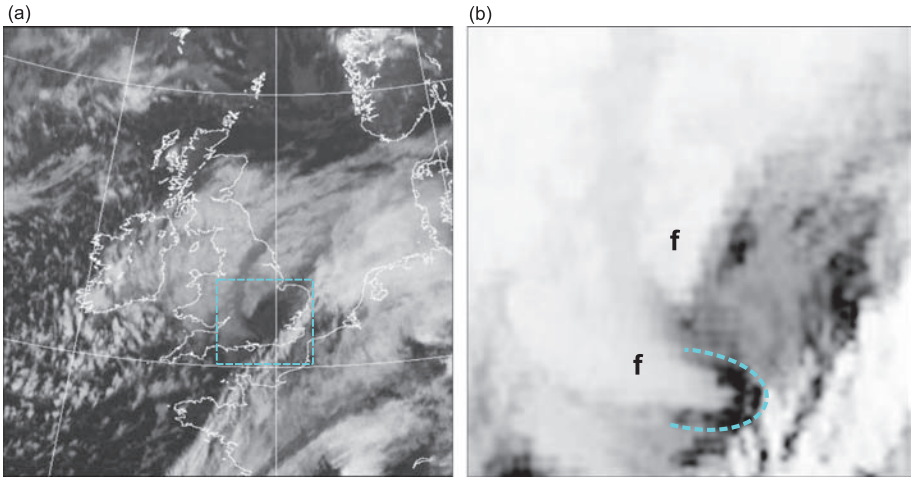


**Figure 3.** (a) Rectified MSG (*Meteosat* Second Generation) 10.7 μm IR image at 0600 UTC on 28 October. The zoomed-in area in (b) is shown by the dashed box. (b) Zoomed-in and enhanced area of (a), showing two major cloud-head filaments, both labelled 'f'. The leading edge of a dark 'chevron' (see Figure 4 and text) is shown by the dashed curve. The focus of this study is on the small region of central southern England near the tips of the cloud filaments constituting the cloud head. (Image courtesy and copyright *EUMETSAT*/Dundee Satellite Receiving Station.)

## 3. Synoptic overview

The St. Jude's Day storm formed as a wave depression in the western North Atlantic on 25 October 2013. It then moved rapidly eastnortheast, deepening from 1004 hPa at 0000 UTC on 27 October to 981 hPa at 0000 UTC on 28 October, a drop in central pressure of 23 hPa in 24 h (see Figure 2). Subsequently a fall of 14 hPa occurred between 0000 UTC (hereafter all times are UTC) and 1200 UTC on 28 October as the storm centre crossed southern England and passed into the southern North Sea. The infrared (IR) satellite image in Figure 3(a) shows the storm at 0600. A polar-front cloud band extends from Biscay and northwest France to Denmark. Much of the UK is covered by the cloud head of the storm, with two major filaments of cloud forming hook-like features terminating over central southern England within the dark dry slot. Figure 4 depicts the corresponding distribution of rainfall given by the operational weather radar network. It shows a large area of rain produced by the cloud head, with embedded bands of heavier rain. The rain band associated with one of the cloud-head filaments terminated close to the 60 km range ring north of the Chilbolton radar and the rain associated with another cloud filament extended over Chilbolton, terminating 40 km ahead of it. There is more banded substructure within the rain area further back under the main cloud head, but it is the rain bands that terminated at the tips of the cloud head that are relevant to this study. Most of the observational analysis will focus on the region near the tip of the filament of cloud and rain that extended over Chilbolton at 0600.

The dashed lines in Figures 3(b) and 4 represent the leading edge of a relatively dark (implying reduced cloudiness) chevron-shaped area ahead of the cloud filament that can be seen in the IR image in Figure 3(a) and more clearly in the enhanced zoomed-in image in Figure 3(b). Chevron features have previously been identified by Browning and Field (2004) near the tips of cloud-head filaments in the Great Storm of October 1987, although in that storm the term 'chevron' was used to describe arcs of elevated boundary-layer cloud believed to have been due to convergence at the leading edges of chevron-shaped regions of suppressed cloud. The detailed analyses presented later in this article are concerned with identifying the physical processes that were taking place in this small region whilst it was close to the Chilbolton radar. It is in this region, just ahead of the evaporating cloud filament tips and in the time period 0500–0900, that some of the strongest wind gusts occurred in the UK. A gust of 29.9 m s$^{-1}$ at 0542 was recorded by the AWS located at the Chilbolton observatory site as the wind direction began to veer from southwesterly to westerly and air temperature and relative humidity dropped and surface pressure rose. Gusts exceeding 25 m s$^{-1}$ were reported quite widely in a swath across the densely populated areas of central southern to eastern England, causing disruption to transport, damage to infrastructure and a number of fatalities.

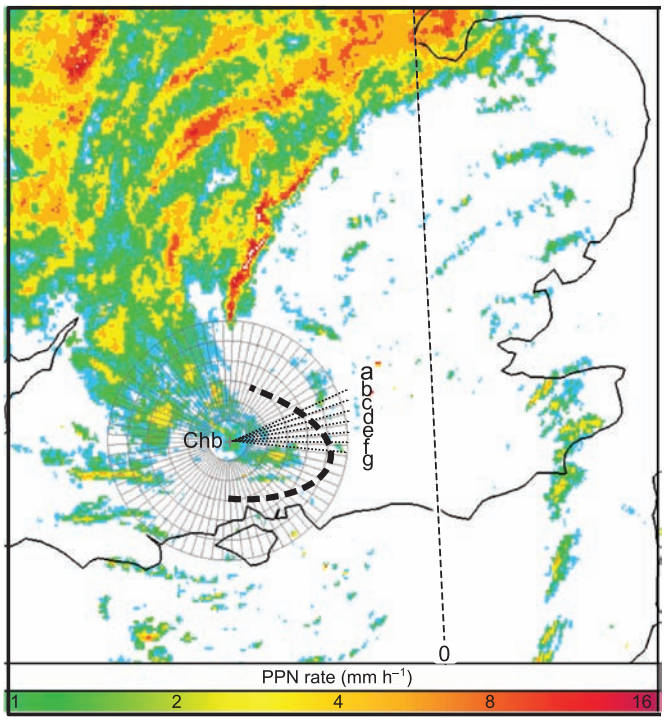


**Figure 4.** UKMO network radar image at 0600 UTC on 28 October. Range rings (every 10 km) and radials (every 5°) centred on the location of the Chilbolton radar (Chb) are overlaid. The scans (a)–(n) in Figure 8 are indicated as dashed black lines, which have been adjusted in this figure to allow for the few minutes delay between these scans and the time of the network radar image. The leading edge of the satellite-detected dark area ('chevron') in Figure 3 is delineated by the bold, dashed black line.

## 4. Mesoanalysis of the strong-wind region using AWSs

Surface analyses generated from the time-composited AWS data show that the strongest 1 min mean wind speeds ($> 18$ m s$^{-1}$) were confined to a relatively narrow swath, typically 30–50 km wide, on the southern flank of the low-pressure centre. The analysis for 0600 in Figure 5 shows the swath of strong winds (red shading in Figure 5(a)) emanating from the tip of the sharply defined bent-back front and entering the frontal fracture region where the contours of $\theta_w$ (dotted contours in (b)) spread out. Comparison with Figures 3 and 4 shows that the western end of

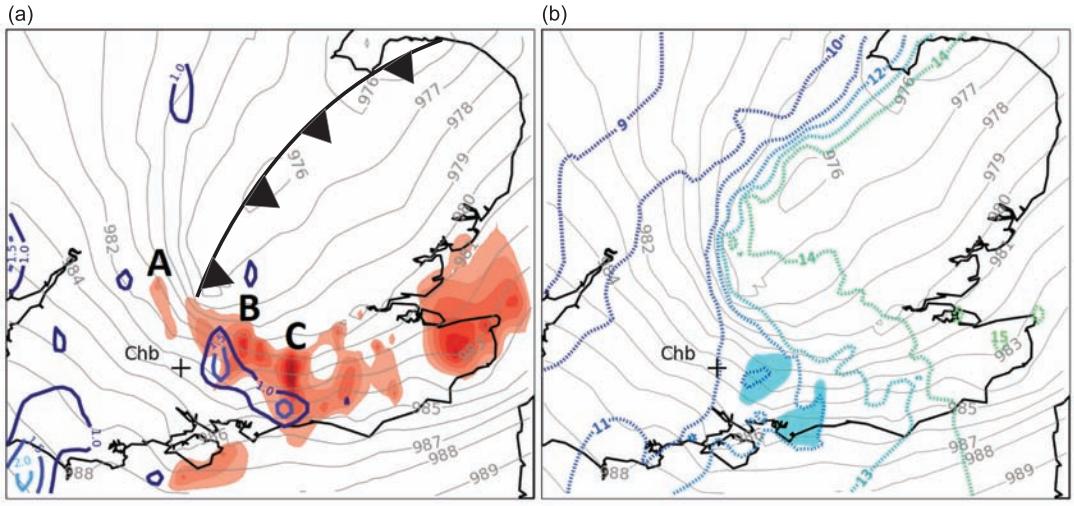


**Figure 5.** The surface wet-bulb potential temperature ($\theta_w$), pressure (SLP), relative humidity (RH) and mean wind speed at 0600 UTC on 28 October, as observed by the AWS network. (a) Red shading denotes wind speeds $>18\,m\,s^{-1}$ with darker shading at $2\,m\,s^{-1}$ intervals above this threshold; grey contours denote SLP (hPa) at 1 hPa intervals; bold, coloured contours denote horizontal divergence, every $0.5 \times 10^{-4}\,s^{-1}$ starting at $1.0 \times 10^{-4}\,s^{-1}$. The position of the BBF (Bent-Back Front) near the surface is denoted by the cold front symbols. A, B, C denote the three wind maxima that are tracked in Figure 6. (b) Cyan filled regions denote RH <75%, dashed contours denote $\theta_w$ (C) at 1 C intervals, SLP contours are as in panel (a). The location of the Chilbolton radar is shown by the cross in (a) and (b).

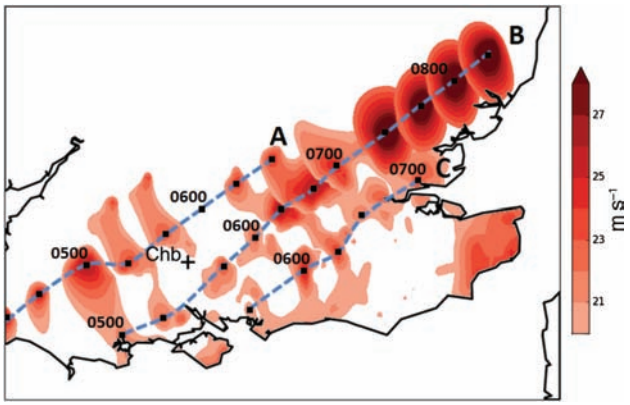


**Figure 6.** Tracks of surface wind speed maxima 'A', 'B' and 'C' over the period 0420–0820 UTC. Red shading denotes regions with mean wind speed $>20\,m\,s^{-1}$, as analyzed from the gridded AWS data at 20 min intervals through the period. Darker red shading is used for wind-speed increments of $1\,m\,s^{-1}$ above $20\,m\,s^{-1}$. Black squares indicate the centroid of each wind maximum at 20 min intervals; dashed blue lines indicate the track of each maximum. The location of the Chilbolton radar is shown by the cross. Times are in UTC.

the swath was located close to and downwind of the filaments of cloud and rain at the tips of the cloud head. Close to and just behind the axis of the strongest winds, the air became drier, with pockets of relative humidity below 75% (cyan shading in (b)). Analyses from the AWSs indicated that the dry air tended to be associated with horizontal divergence in the surface wind field (blue contours in (a)). The location of the dry divergent surface air corresponds to the chevron feature discussed above in connection with Figures 3 and 4.

Figure 6 shows the areas of strong winds moving rapidly northeastwards across southern England (translating at a mean velocity of $21.4\,m\,s^{-1}$ from 233°). Within the swath of strongest surface winds, at least three individual wind maxima were resolved, each around 15–25 km wide (labelled 'A', 'B' and 'C' in Figures 5(a) and 6). At many AWS sites, the peak gust occurred as one or other of these features moved across the site; indeed, almost all inland gusts $>30\,m\,s^{-1}$ were found to have been associated with these features. The density of wind observations over southern England is generally not sufficient to permit a detailed analysis of the evolution of individual maxima. However, observations are sufficiently dense for the paths of the centroids of the wind maxima to be tracked, for periods of about 2 or 3 h, as they move northeast across the area. After about 0700, the strongest winds moved into an area of relatively sparse observations over eastern England. Consequently, the analyses do not capture the detailed structure of the area of high wind speed after this time (e.g. note the apparently ovoid shape of maximum 'B' after 0700 in Figure 6, which is likely a consequence of sampling by only two AWS stations during this period). However, at earlier times, including the critical period of study when the strongest winds were near Chilbolton, the swath was sampled better. The existence of areas of slightly weaker winds between areas 'A', 'B' and 'C' is confirmed by observations from AWSs that lay between the tracks of the maxima in the period 0500–0700, increasing confidence in the diagnosis of three individual maxima within the swath of strong winds at this time.

Figure 7 shows the surface wind field derived from the AWSs (contours) superimposed on the Doppler velocity from the lowest-elevation scan of the Chilbolton radar just before ((a), at about 0528) and just after ((b), at about 0553) the strongest winds had passed over Chilbolton. Bearing in mind that the radar measures radial velocity some distance above the ground, the qualitative correspondence between the radar and AWS analyses is reassuring. The bold arrow in Figure 7(a) shows the track of a $22\,m\,s^{-1}$ wind maximum corresponding to strong wind area 'A'. The bold arrow in the right-hand panel (Figure 7(b)) shows the track of the separate $22\,m\,s^{-1}$ wind maximum (actually split into two cores at this time) that was identified in Figure 6 as Area 'B'. This is the area of strong winds that will be analyzed in detail in section 5. A $34.8\,m\,s^{-1}$ gust occurred at Odiham, near the northern flank of maximum 'B' (~35 km eastnortheast of Chilbolton), at 0553. The same wind maximum was also responsible for $>30\,m\,s^{-1}$ gusts in the west London area around 0620–0640 (including $30.7\,m\,s^{-1}$ at Heathrow and $30.3\,m\,s^{-1}$ at Northolt, both at 0636).

## 5. Structure of the lower atmosphere above the region of strong surface winds in Area 'B' as inferred from radar

In this section we examine data from the Chilbolton radar when the region of strong surface winds, identified in section 4 as Area 'B', was close to the radar. We first show, in section 5.1, that the strong surface winds were beneath a part of the LLJ where shallow convective showers were decaying and then, in section 5.2, we examine the nature of the convection.

### *5.1. Evidence of evaporating convective showers above the Area 'B' region of strong surface winds*

Figure 8 shows a set of RHI scans at 5° intervals from 065° to 095° (all azimuth angles are with respect to north) obtained by the

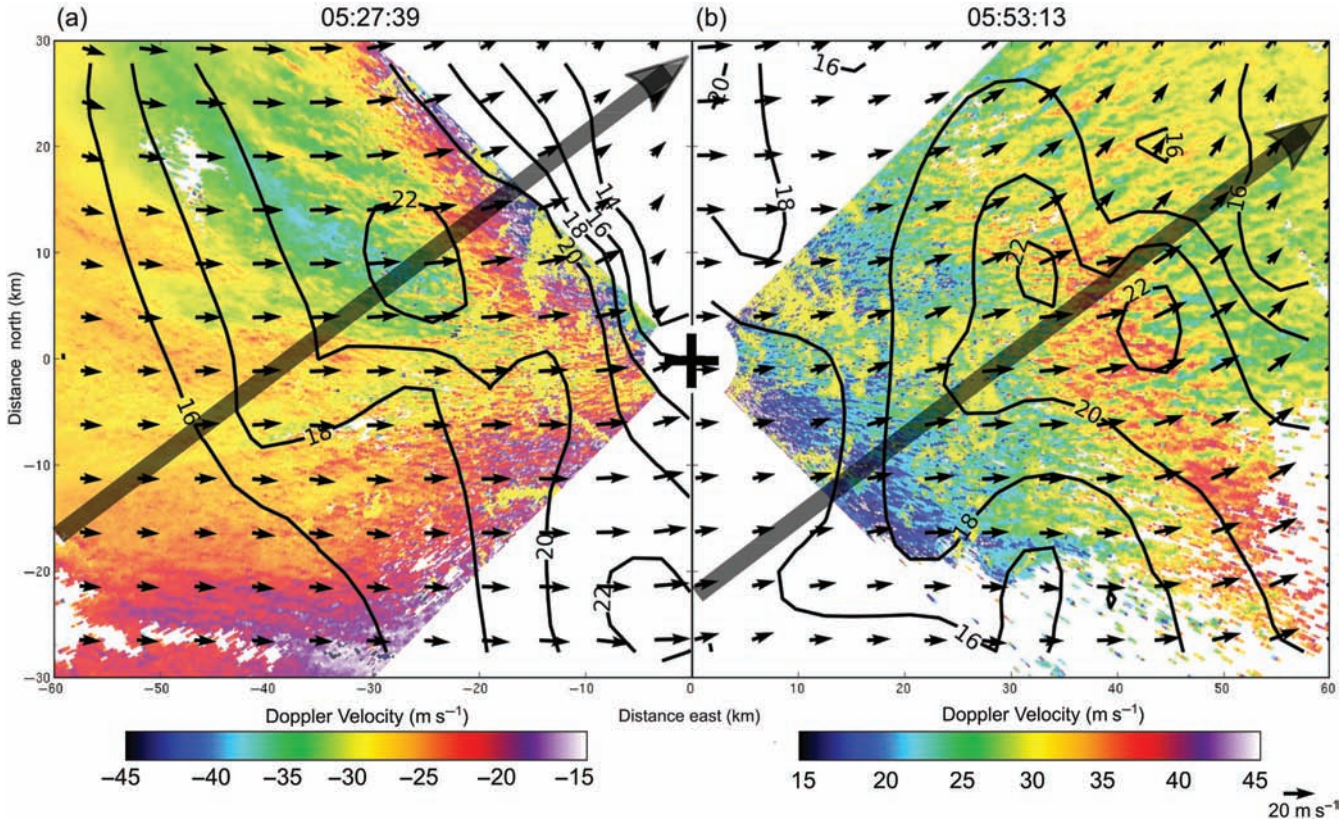


**Figure 7.** The near-surface wind field just prior to and after passage of the LLJ maxima over Chilbolton. CAMRa Doppler velocity PPI scans at 0.5° elevation (radial component of the wind speed shaded; m s$^{-1}$) overlaid with the 2 m wind field derived from AWS observations (contours of mean wind speed every 2 m s$^{-1}$ and flow vectors every 5 km). (a) Westward-looking scan at 0528 UTC and (b) eastward-looking scan at 0553 UTC on 28 October. The location of the Chilbolton radar is marked by the bold '+'. Two bold arrows are drawn to indicate the inferred motion of two separate velocity maxima, 'A' (in (a)) and 'B' (in (b)) (see text).

Chilbolton radar at times between 0555 and 0558. The locations of these scans (adjusted for the few minutes delay between them) were shown earlier in Figure 4. Comparing Figures 4 and 5(a) shows that these RHI scans in Figure 8 were within the region of strong winds associated with Area B. Radar reflectivity is shown in (a)–(g) and radial velocity in (h)–(n). Although much of the region of strong winds corresponding to Area B was just outside the main areas of precipitation and in or close to the chevron-shaped region of suppressed cloud and low radar reflectivity, nevertheless the sensitive Chilbolton radar was able to detect a significant amount of radar echo in this region. Some of the echo, with reflectivity shown violet ($Z < -5$ dBZ), is likely to have been due to refractive-index inhomogeneities at the boundaries of convective cells. For example, as we demonstrate in section 5.2, the undulating violet echo region centred at an altitude of about 700 m marks the top of the convective boundary layer (see, for example, 'a' in Figure 8(c) and (f)). However, it is the low-reflectivity region from about 700 m to 3 km between ranges of about 10 and 50 km that we shall concentrate on first. Whilst some of the violet echo within this layer may have been from the boundaries of shallow elevated convection (evidence for which is presented in section 5.2), there are other, slightly more intense (green), echoes aloft that would have been due to patches of residual precipitation associated with this convection (see, for example, 'b' in Figure 8(a), (d), (f) and (g)). Although some rain shafts on the edges of the low-reflectivity region reached the ground (for example, 'd' in Figure 8(b) and (g)), we shall go on to confirm this to be a region of evaporating shallow showers.

There is a zone, about 20 km wide in the RHIs in Figure 8, corresponding to the dark chevron, where the evaporation has eliminated all except a few isolated shafts of precipitation. The velocity plots in the right-hand column show that the detectable boundary of the zone of maximum evaporation is characterized by the strongest observed winds and it is believed that the almost echo-free zone within this boundary corresponds to the core of the LLJ. Later, in section 6, we shall present evidence from a well-validated run of the WRF model that parcel trajectories in this LLJ did indeed have a recent history of descent within evaporating cloud. Similar RHI scans made earlier when Area B was upwind of Chilbolton indicate a similar pattern, albeit with a little more precipitation echo, because the evaporation had had less time to deplete the precipitation. (One such RHI is shown later in Figure 17.) We are therefore beginning to arrive at a picture in which the LLJ above the area of strong surface winds coincides with recent and some ongoing evaporation of elevated shallow convective showers.

### 5.2. *Nature of convection in the Area 'B' region of strong winds*

#### 5.2.1. *RHI evidence of different types of convection*

The set of RHI scans presented in the previous section was selected because it was relatively free from echoes due to ground-clutter. There was some clutter (see, for example, 'c' in Figure 8(b), (d), (i), (k) and elsewhere) and some of the side-lobe returns extended up to 2 km and above (see yellow columns labelled 's' in Figure 8(k)), but they do not obscure the main information elsewhere. Another set of scans through Area 'B', made several minutes earlier, was badly contaminated by clutter, probably because of anomalous propagation immediately following the passage of a brief shower at the radar site, the outflow from which would have contributed to the pool of diverging dry air at the surface shown in Figure 5(a). One of the RHI scans from the Chilbolton radar during this earlier cycle was, however, relatively free from clutter and, since it happened to be a very informative scan, we shall use it now to examine the nature of the convection in more detail. The RHI scan towards 110° at 0548 is shown in Figure 9. Figure 9(a) and (b) show the reflectivity and Doppler velocity plots, respectively, and Figure 9(c) shows tracings highlighting the following four key features inferred from (a) and (b). Note that the interpretations of these features that follow will be supported by our analysis of the convective patterns in plan view, which are

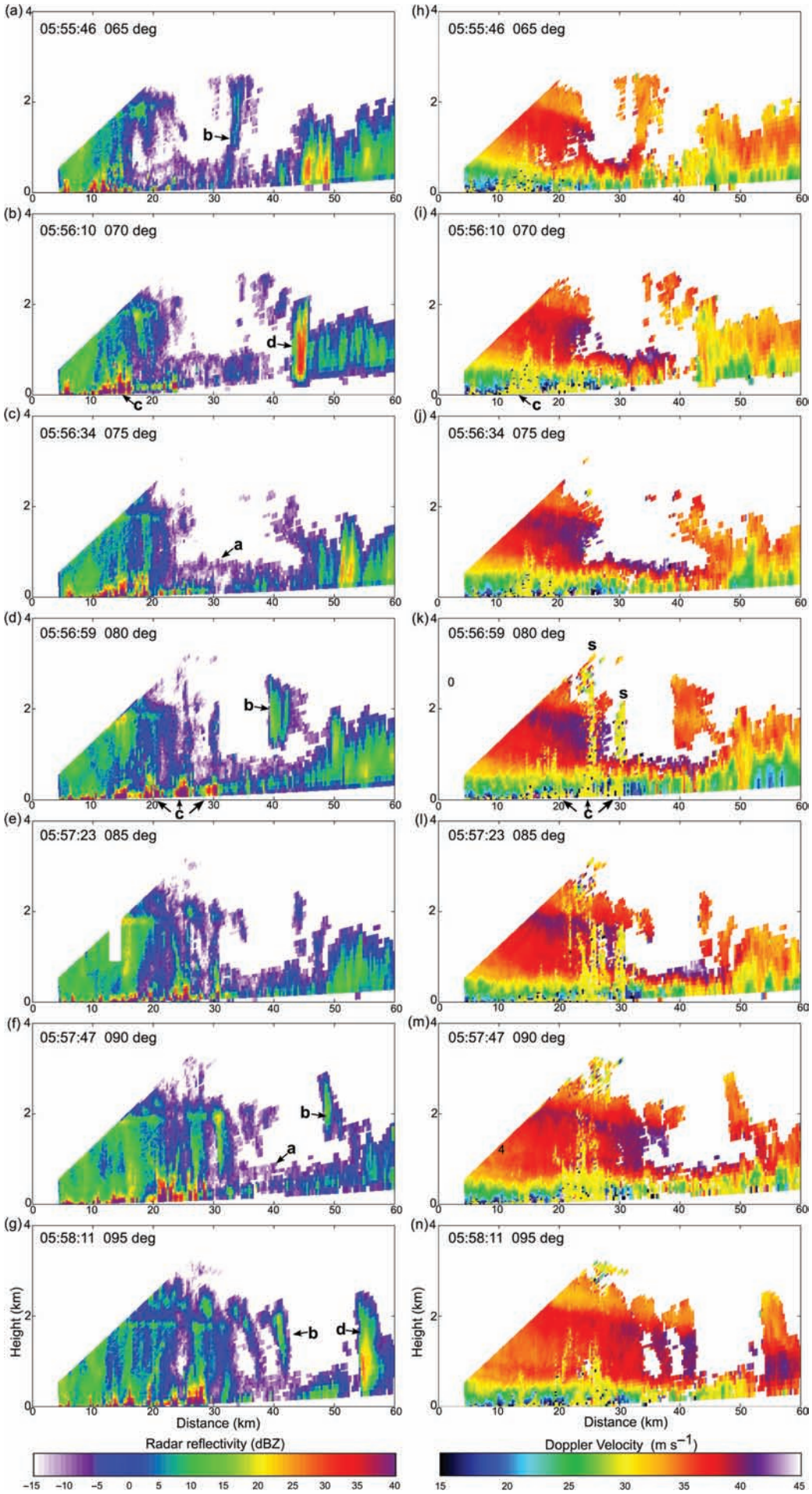


**Figure 8.** (a)–(n) CAMRa RHI scans at 5° intervals from 065° to 095° (from north) for times between 0555 and 0558 UTC on 28 October. Radar reflectivity is shown in (a)–(g) and Doppler velocity in (h)–(n). (The red and yellow echoes in the lowest 500 m out to 30 km range in the reflectivity plots are due to ground returns. The more vertically extensive yellow columns in some of the Doppler velocity plots, especially between ranges 23 and 31 km in (k), (l), (m) and (n), are due to side-lobe returns from ground clutter.) See text for explanation of labels a–d and s.

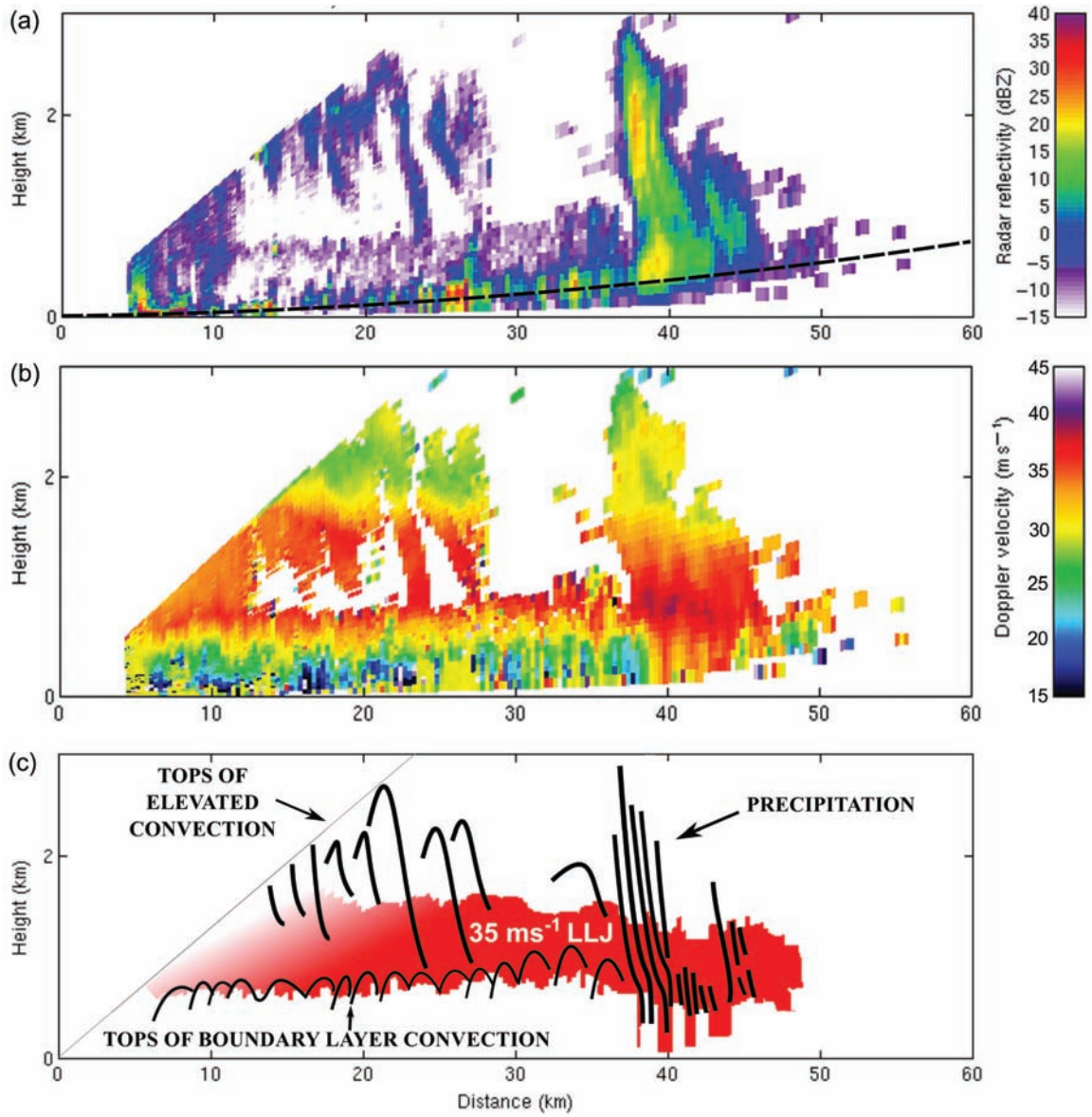


**Figure 9.** (a)–(c) CAMRa scan at 0548 UTC on 28 October towards 110° (from north). (a) Reflectivity (dBZ); (b) Doppler velocity ($m\,s^{-1}$); (c) schematic showing the LLJ with velocity exceeding 35 $m\,s^{-1}$, shaded in red, and tracings of the vertical extent of elevated and boundary-layer convection and precipitation shafts inferred from (a) and (b) (see text). The approximate location of the radar beam at 0.5° is shown by the dashed line in (a).

shown later in Figure 11. The four features labelled in Figure 9(c) are as follows.

(1) Tops of boundary-layer convection, at heights of around 700 m but rising to 1000 m at 35 km range. These have been inferred from the wave-like violet echo seen most clearly between 11 and 23 km range in Figure 9(a). The wave-like nature of the boundary-layer top is also evident in the pattern of vertical wind shear shown in Figure 9(b) and it is this that gives us confidence to extend our depiction of the boundary-layer top in Figure 9(c) to 38 km range, where the reflectivity pattern is more confused. Later, in Figure 11, we show that the boundary layer is characterized by longitudinal rolls. Since the section in Figure 9 is orientated roughly along the axis of these rolls, the wave-like nature of the boundary-layer top evident in this figure is probably representative of turbulent eddies along the wind direction within the rolls rather than the rolls themselves.
(2) Tops (and edges) of elevated convective cells occupying the region above the boundary layer up to about 2500 m. These have been inferred from the echo pattern in the reflectivity plot in Figure 9(a).
(3) Shafts of precipitation associated with the shower at around 40 km range derived from the reflectivity plot in Figure 9(a). (This is the shower referred to as Shower '2' in Figure 10.) .
(4) A LLJ with velocity component in excess of 35 $m\,s^{-1}$ extending from the top of the boundary layer to about 1.5km (shaded red). This is based on the Doppler plot in Figure 9(b) plus some interpolation across regions of weak or no echo,† which are believed to have been affected by a combination of decaying convection and evaporation. Evidence from other RHIs (e.g. Figure 12, later) supports the view that this weak-echo region corresponds to the core of the LLJ.

*5.2.2. Evidence of convective showers bringing down high momentum to the surface*

A noteworthy feature of Figure 9 is the extension of the strong-wind region towards the ground within shafts from 40–44 km range associated with the shower at these ranges. We cannot tell from the radar alone that these shafts of strong wind actually reached the ground, because the base of the beam was about 200 m above the surface at this range; however, AWSs support the view that the strongest gusts did indeed coincide with the

†Post-processing of the raw radar data to remove the noise also removes some signal. Inspection of the raw images (not shown) reveals sufficient patches of high-velocity signal to suggest that this region corresponds to the jet core.

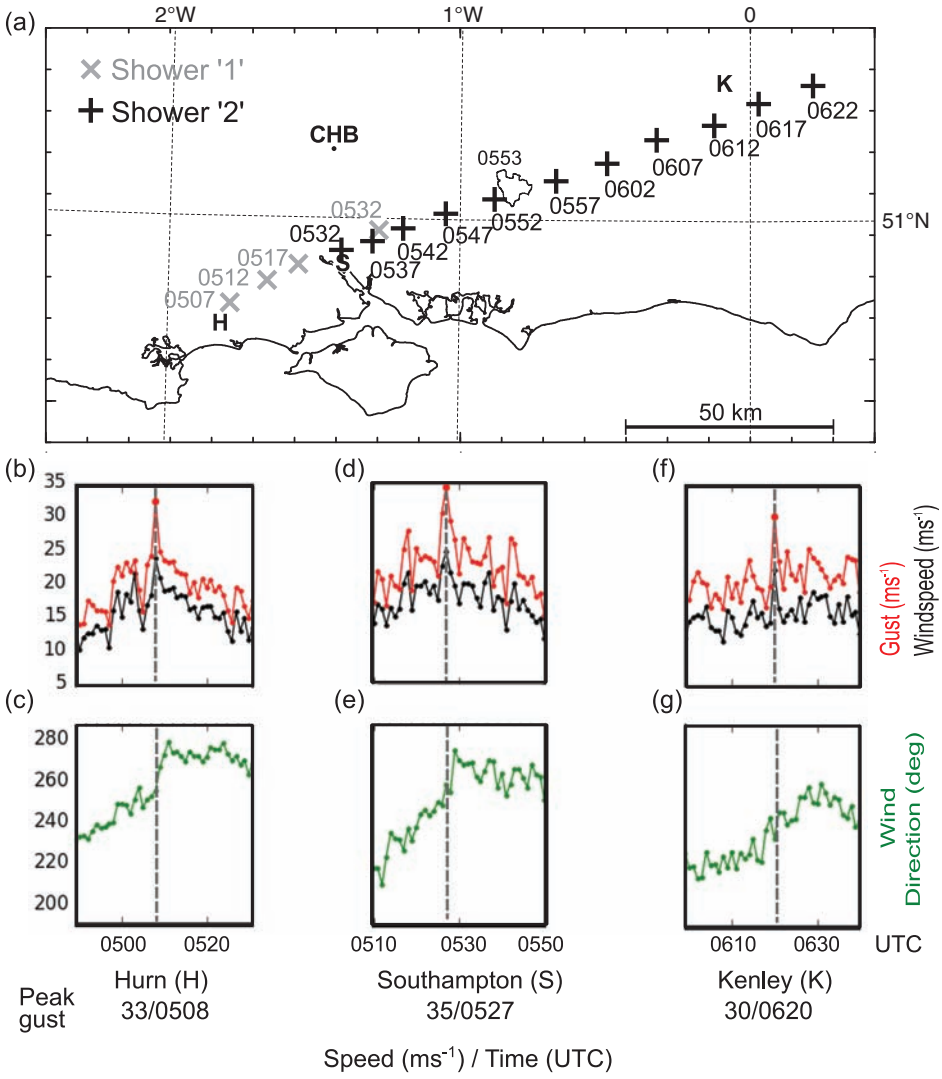


**Figure 10.** The tracks of showers observed by the operational radar network. (a) The locations of shower '1' and shower '2' at 5 min intervals are indicated by × and + symbols, respectively. The ∼0 dBZ reflectivity contour of shower '2', detected by the Chilbolton radar (CHB), is shown at 0553 UTC. The locations of three AWS sites (Hurn, Southampton and Kenley) are also indicated. Panels (b), (d) and (f) show plots of wind gusts (upper trace) and mean wind speeds (lower trace). Panels (c), (e) and (g) show plots of wind direction (degrees from north) from the AWSs. The times of the peak wind gusts, related to the passage of a shower nearby, are indicated by the thin, dashed, vertical lines.

passage of two showers. Figure 10(a) shows the position of these showers at 5 min intervals between 0507 and 0622, as determined from the Chilbolton radar and the operational radars at Dean Hill and Chenies. Plots in Figures 10(b–g) of the 1 min wind from three AWSs within ∼10 km of the centre of a shower track show that at each station the peak wind occurred within 3 min of the passage of a shower. The shower passage is particularly well marked in the gust records, as one would expect from a downdraught/downburst-induced outflow. The peak gusts occurred as the wind was veering, but between 2 and 11 min before the time of maximum veer. As we see later (section 6) from an analysis of model output, the veering of the wind was associated with the arrival of the leading edge of a CJ at the surface, which was undercutting a SJ at the level of the main LLJ. The wind direction at the time of the peak gusts was 260° or less, which, according to the model, corresponds to the wind direction in the SJ (refer ahead to Figure 15 (b and c)).

### 5.2.3. *PPI evidence of linear organization of the convection*

An interesting feature of the convection in the region of strongest winds is its linear organization, as revealed by PPI scans with the Chilbolton radar. Figure 11(a) shows the pattern of Doppler velocity in the PPI sector scan at 0553. Fortunately, much of the scanned sector is within 30° of the wind direction and so the radial Doppler velocities are a reasonable approximation of the true wind speeds. As is clear from the dashed line depicting 0.5° elevation in Figure 9(a), the elevation of the PPI scan in Figure 11(a) and (b) was such that it represents velocities entirely within the boundary layer. To help understand what Figure 11(a) shows, we have defined two areas in this figure, labelled 'I' and 'II', characterized by different kinds of banding. The spacing of the bands was determined by manual analysis of zoomed-in plots. The different pattern of Doppler velocity in each of these areas reveals information about the nature of the convection.

**Area I:** This is characterized in Figure 11(a) by narrow west–east bands of blue echo (20–25 m s$^{-1}$) separated by very pale blue echo (∼15 m s$^{-1}$), corresponding to longitudinal rolls of convection. The patches of green echo[‡] obscuring the blue bands in places are due to ground clutter which, as mentioned before, was anomalously bad at this time. The bands that are blue are likely to correspond to descending higher-velocity air and the very pale blue bands correspond to ascending lower-velocity air, as part of the helical circulations within the longitudinal boundary-layer rolls. The spacing of these bands is 700 ± 300 m and this is

[‡]Green echo, according to the key in Figure 11, corresponds to a velocity of 30 m s$^{-1}$; however, the range of unambiguous Doppler velocity for the Chilbolton radar is such that this colour also represents ground clutter returns with a velocity of 0 m s$^{-1}$.

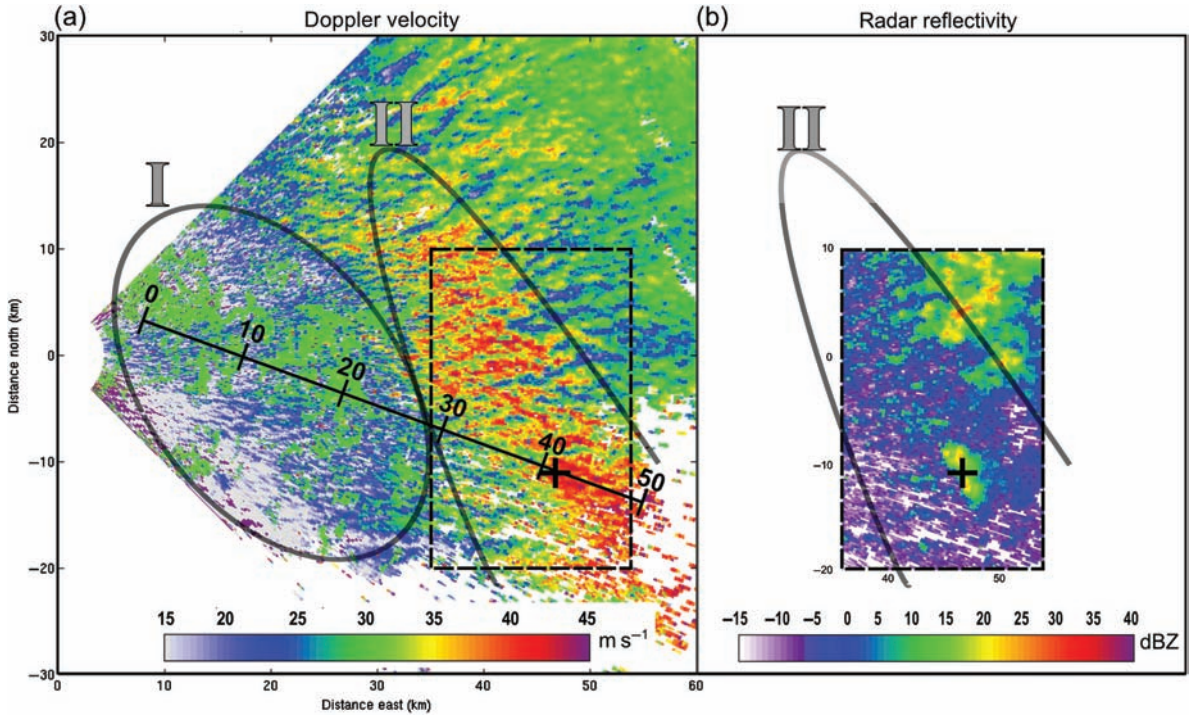


**Figure 11.** CAMRa PPI scan at 0553 UTC on 28 October. (a) Doppler velocity (m s$^{-1}$) shaded. The image has been enhanced and the approximate areas of two types of convective circulation I and II have been outlined (see Table 1 below and text). A line showing the position of a 50 km long section of the RHI scan in Figure 9 has been superimposed, with a displacement compensating for the time difference between the scans. (b) Radar reflectivity (dBZ) within the rectangular frame drawn in (a). The centre of the shower highlighted in Figure 9 and identified in Figure 10 as Shower '2' is indicated by a bold cross in (a) and (b).

consistent with what might be expected in view of the observed depth of the boundary layer, which was 800 ± 300 m according to Figure 9. Similar boundary-layer rolls have been observed by means of dual-Doppler analyses in a hurricane by Kosiba and Wurman (2014) and are discussed by Li *et al.* (2015).

**Area II:** This is the region near the tip of the dark chevron (Figure 3) where the strongest winds were reaching the ground. It is characterized by rather irregular, but significantly more widely spaced, longitudinal bands. The orange–red coloured parts of these bands in Figure 11(a) correspond to velocities of over 35 m s$^{-1}$. This is slightly higher than the gust velocities recorded by the AWSs (cf. Figure 10). It is not easy to define a spacing for these bands, but a rough indication is 2000 ± 1000 m. This is more than twice the width of the boundary-layer rolls elsewhere and is compatible with the convection being much deeper and extending from the surface up to the 2500 m tops of the convective echoes, which is consistent with the above inference that the shower at about 40 km range was bringing high momentum from the LLJ above the boundary layer down to the surface. (Figure 11(a) shows that the region of widely spaced convective rolls actually extended beyond Area II, to the north and east. There, however, the near-surface winds were not as strong because the convective showers occurring in this region were ahead of the leading edge of the LLJ core.)

The upper-level convective cells shown in Figure 9 at ranges closer than 40 km, which no longer exhibit any detectable precipitation echo, are decoupled from the boundary layer and extend from the boundary-layer top at 700 m to about 2500 m. In the light of the earlier discussion and as supported by the parcel trajectories derived from the model in section 6, we believe that these convective cells had previously produced precipitation that had evaporated over the previous hour or so. It is likely that the shower at 40 km range, which is highlighted in Figures 9–11, began similarly as elevated convection but persisted longer, having developed a more vigorous downdraught which, aided by shearing instability, penetrated the boundary layer and reached the ground. Similar downdraughts were probably responsible for the shafts of high velocity extending beneath the shower observed around 56 km range in Figure 8(n) and elsewhere.

In summary, we have identified three different categories of convection from a combined analysis of the RHI and PPI scans: (i) longitudinal rolls of convection in the boundary layer (best seen in Area I in Figure 11(a)), (ii) upper-level or elevated convection (with unknown organization in plan view, because no PPI scans were made through these levels) and (iii) irregular longitudinal rolls of penetrative convection (in and beyond Area II). Some of the strongest surface winds occurred where the penetrative convection coincided with the core of the LLJ, as in Area II in Figure 11(a). The properties of these three categories of convection are summarized in Table 1.

### 5.2.4. *An unresolved issue*

The above summary is valid up to a point, but in one important respect it is an oversimplification. Not all of the places experiencing strong near-surface winds and coloured orange–red in Figure 11(a) were associated with ongoing showers resembling the one near 40 km in Figure 9.

Figure 11(b) depicts radar reflectivity in the part of Area II defined by the boxed subregion in Figure 11(a). The boundaries of this region have been drawn to exclude the ground-clutter echoes that contaminated the data at closer ranges. Figure 11(b) shows that, whilst some of the strong winds in Area II are associated with significant showers (see the echoes highlighted by the cross), much of the strong-wind area is (as also shown by Figure 8) where the showers are very weak and few and far between. As noted earlier, the violet echo (and perhaps the blue echo too) is mainly due to refractive-index inhomogeneities rather than precipitation and even some of the smaller green echoes may not have been due to showers. (Alternating rapidly between images indicates a negative correlation between strong winds and echo intensity in many places outside the shower highlighted by the cross, suggesting that most of the small green echo maxima in Figure 11(b) are associated with the rising parts of boundary-layer

Table 1. The properties of the types of convective circulation seen in Figures 9 and 11.

| Location | Type of convection | Depth of convection (m) | Spacing of lines (m) |
|---|---|---|---|
| Area I | BL convection lines | $800 \pm 300$ | $700 \pm 300$ |
| Area II | Penetrative convection | $2500 \pm 500$ | $2000 \pm 1000$ |
| Above parts of Areas I and II | Elevated convection | $1700 \pm 200$ | – |

circulations bringing up low momentum and perhaps some particulates disturbed from the surface by the neighbouring bands of strong winds.)

It is evident therefore that, although the very strongest surface winds were associated with ongoing showers, fairly strong winds also penetrated towards the ground in places where vertically extensive shafts of rain no longer existed. A vertical section illustrating this is shown in Figure 12(a) and (b). This figure depicts an annotated and enlarged view of one of the RHI scans shown earlier as part of Figure 8. The pale grey dashed line in Figure 12, derived from the model as discussed later in section 6, shows where the LLJ was descending by more than 30 cm s$^{-1}$ in the form of two sting jets, SJ and SJ′. The part of the LLJ in Figure 12 centred at a height of 1000 m that is devoid of echo between 25 and 45 km is where almost all traces of earlier elevated convection have decayed; all that can be seen at these ranges is boundary-layer echo with tops to 700 m, together with some residual precipitation aloft left over from earlier elevated convection. Nevertheless, Figure 12(b) shows filaments of high velocity extending towards the ground at ranges 38–47 km as part of circulations that were effectively engulfing air from above the boundary-layer top. We hypothesize that this engulfment was possible because the weak-echo parts of the LLJ above the boundary layer had been cooled sufficiently by the evaporation of precipitation generated by the previous elevated convection.

We cannot be certain that these high velocities necessarily reached all the way to the surface, as was shown to be the case with the showers, but nevertheless this would account for high velocities reaching down to within a few hundred metres of the surface, as seen in the PPI scan in Figure 11(a), and probably accounts for the fairly high velocities at the surface. The fact that the spacing of the lines of strong winds throughout this region (i.e. Area II in Figure 11(a)) is relatively large even where ongoing showers no longer exist is perhaps surprising and suggests that the horizontal scale of these convective circulations was still being influenced by the scale of inhomogeneities established by the original deeper convection. Whether or not this is the case remains unresolved. The irregularity in the organization of the orange–red lines of strong wind in Area II in Figure 11(a) might indicate the existence of a mix of convective scales, with some deep convection but also some shallower shear-induced circulations involving entrainment at the top of the boundary layer.

## 6. Interpretation of the LLJ observed just above the boundary layer using NWP model results

In the previous section, we showed that the strongest surface winds were due to convection bringing down momentum from a LLJ located in a shallow region of descent just above the boundary layer. A LLJ that produces strong surface winds near the tip of

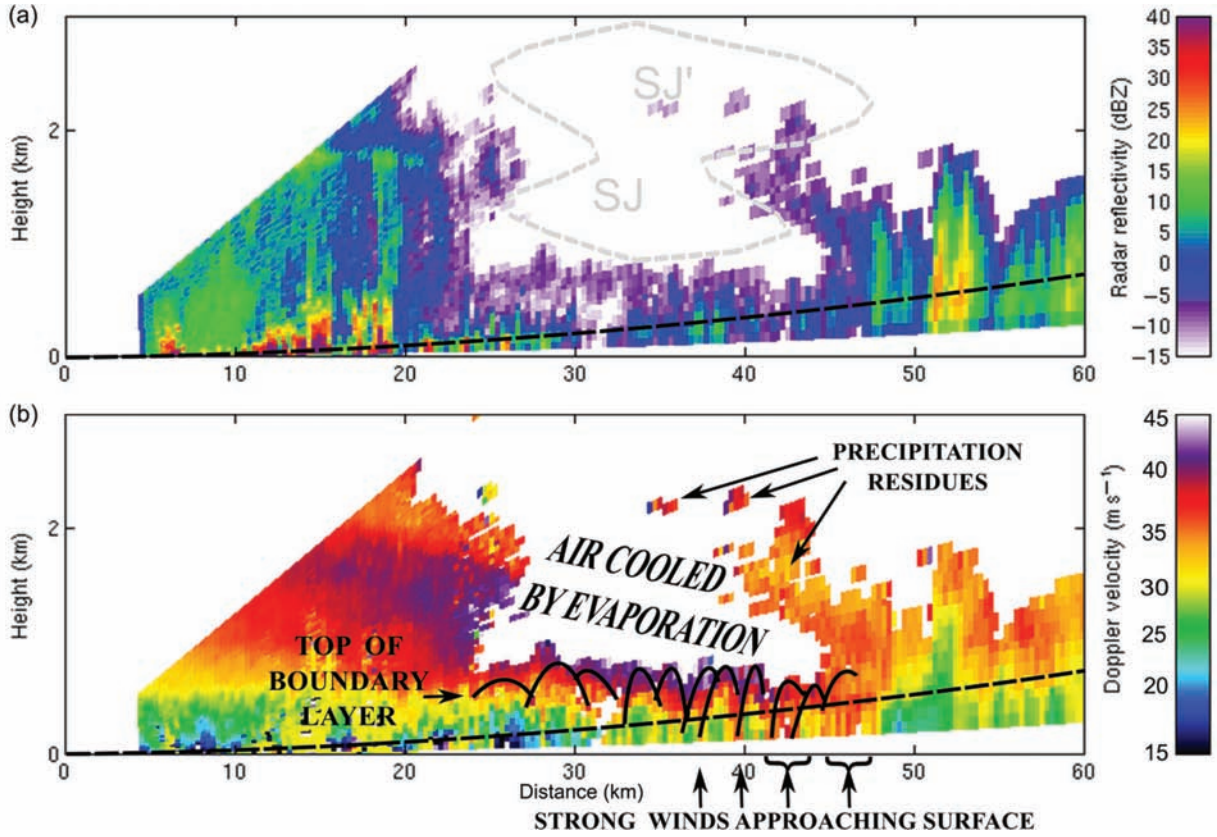


**Figure 12.** CAMRa RHI towards 075° (from north) at 0556 UTC on 28 October. (a) Reflectivity (dBZ), shaded. (b) Doppler velocity (m s$^{-1}$), shaded. The approximate locations of the radar beam at 0.5° are shown by the dashed lines. The −30 cm s$^{-1}$ vertical velocity contour (dashed, grey line) from a comparable cross-section of the model run has been superimposed in (a) and the locations of the two sting-jet cores, SJ and SJ′, are annotated as derived from model results presented later in section 6. Panel (b) is annotated to show where the engulfment of high-momentum air deep in the boundary layer is occurring, i.e. where there are no longer any remaining showers but where the evaporation of previous showers has presumably cooled the air in the LLJ sufficiently to increase its density enough for it to be entrained/engulfed further into the BL.

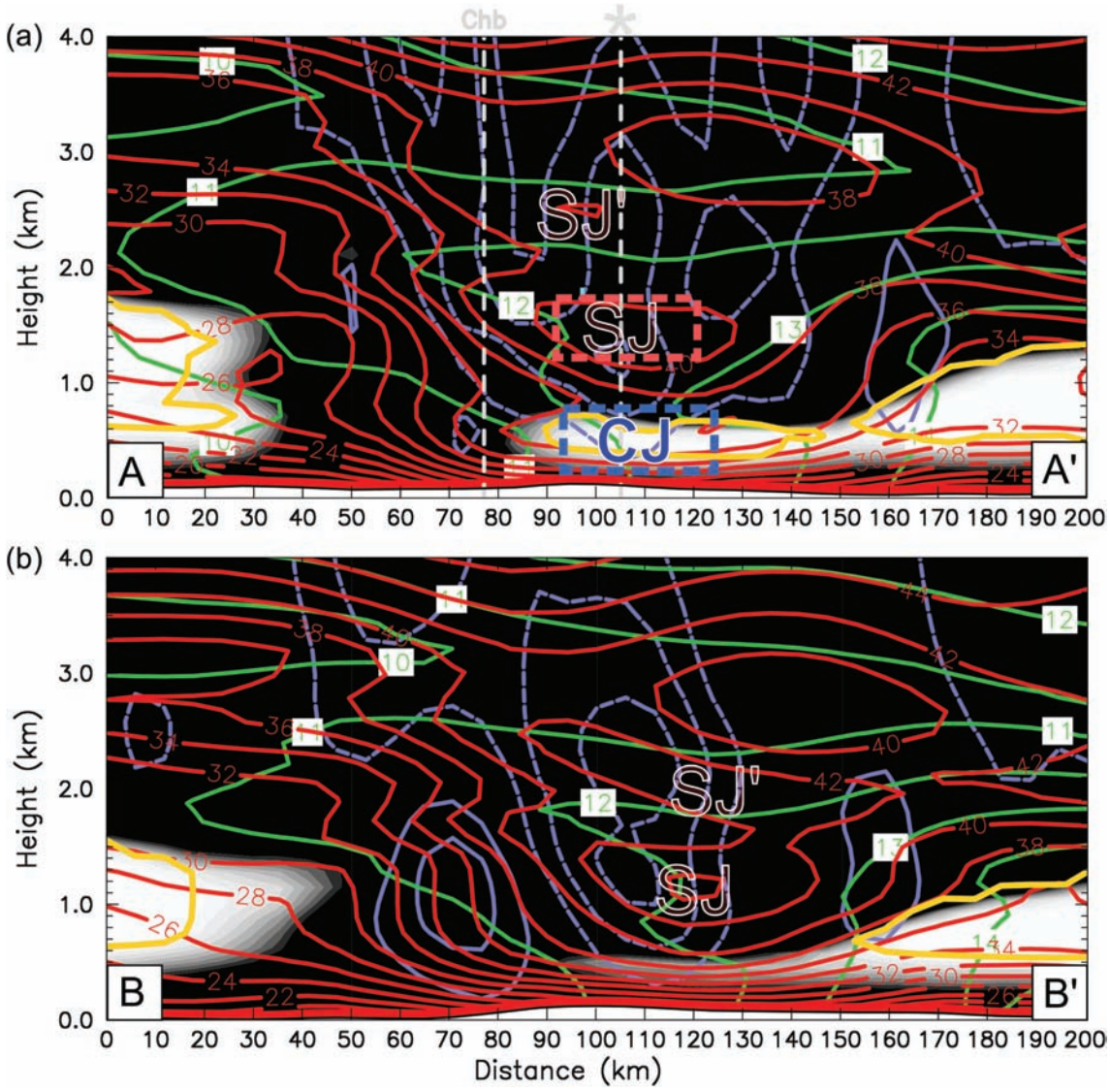


**Figure 13.** Cross-sections showing the vertical structure of the frontal fracture region at 0600 UTC on 28 October. (a), (b) Sections A–A′, B–B′. See Figure 14 for locations. Relative humidity with respect to ice (RHi) (%), shaded from 90%, black to 100%, white; $\theta_w$ (C), green contours with boxed labels every 1 °C; Earth-relative horizontal wind speed (m s$^{-1}$), red contours every 2 m s$^{-1}$; vertical velocity (cm s$^{-1}$), blue contours every 10 cm s$^{-1}$, negative dashed, zero suppressed; cloud mixing ratio (g kg$^{-1}$), gold, bold contour 0.005 g kg$^{-1}$. The locations of the main jet cores (see text) are annotated: CJ, SJ and SJ′. The starting points of the trajectories for each jet (see text and Figure 16) are enclosed by the dashed boxes. The locations of the Chilbolton radar (Chb) and the vertical profiles in Figure 15(b) (*) are shown by the grey dashed vertical lines in (a).

a cloud head can be either a cold-conveyor-belt jet or a sting jet, according to the circumstances (Smart and Browning, 2014), but the fact that the LLJ in the present study is centred above, rather than within, the boundary layer points to it being a SJ rather than a CJ. In order to support this suggestion, we shall now present output from the NWP model run described in section 2.3. Most of the output shown here is for model time 0345 but, as explained in section 2.3, this corresponds to about 0600 in the real world, which is how the following figures will be labelled.

Two cross-sections, AA′ and BB′, are plotted in Figure 13(a) and (b), respectively, the positions of the sections being indicated in Figure 14. Both cross-sections in Figure 13 intersect the region of divergence (see dashed green contour in Figure 14). Three LLJs are labelled in section AA′ (only two in section BB′). In section AA′, they are almost vertically aligned above each other and just to the east of Chilbolton (dashed line labelled Chb). The location of the LLJs is highlighted by the dashed line labelled *. The lowest jet is very close to the surface on the cold side of the remains of the bent-back front and beneath the cold-frontal zone, where it slopes upwards to the left: this suggests that it is a CJ.

The other jets in Figure 13 are sting jets, as we shall confirm shortly from an analysis of trajectories. The principal sting jet (SJ) can be seen descending from a height of 1.5 km in section AA′ to a height of 1.2 km in section BB′. Strictly, this descent can be inferred from Figure 13(a) and (b) only if there is a quasi-steady state structure, but such descent is also confirmed by the trajectory analysis. Meanwhile, as confirmed by the trajectory diagnostics discussed later, its velocity has increased from 40 to 44 m s$^{-1}$, the cloud and precipitation with which it was associated having evaporated during the previous hour (refer ahead to Figure 17). A second sting jet (SJ′), confirmed by trajectory analysis (not shown), is labelled in section AA′ at a height of 2.5 km; it is the tail end of an earlier sting jet that descended to lower levels further ahead of section AA′ (see Figure 14). There is a hint of SJ′ at the top of the precipitation echo in (some of) the CAMRa Doppler plots shown in this article, but there is much clearer evidence for SJ′, as well as SJ, in the Doppler plots for the scanning cycle made 25 min earlier centred on 0530 (not shown). We shall focus on SJ, because it corresponds most closely to the LLJ that was responsible for the strongest surface winds analyzed in section 5.

It is instructive to examine the vertical structure of the lower atmosphere in the vicinity of the CJ and SJ as determined from the model. Tephigrams are plotted in Figure 15 for the three locations shown in Figure 14 by a blue bullet, a red bullet and an asterisk. The sounding at the location of the blue bullet, in Figure 15(a), shows a 35 m s$^{-1}$ SJ centred at 750 hPa and a 30 m s$^{-1}$ CJ

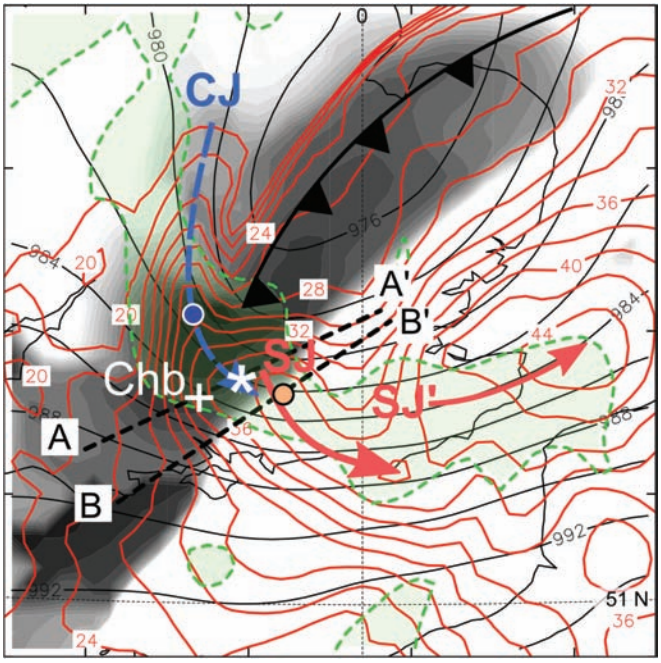


**Figure 14.** Subsection of the model domain at 0600 UTC on 28 October, with model-derived OLR (Outgoing Long-wave Radiation) shaded, from white (200 K) to black (300 K). MSLP is contoured with thin, black lines every 2 hPa; horizontal wind speed at 925 hPa is contoured with lines every 2 m s$^{-1}$ starting at 18 m s$^{-1}$; divergence of 2.5 × 10$^{-5}$ s$^{-1}$ at 925 hPa is contoured with a green, dashed line enclosing a tongue of maximum divergence, shaded pale green, extending roughly along the axis of maximum wind speed. All fields have been smoothed. The positions of the two cross-sections in Figure 13(a) and (b) are shown by the dashed lines A–A′ and B–B′. The location of the Chilbolton radar (Chb) is marked by the white cross. The location of the vertical profiles in Figure 15 are marked by the blue bullet (Figure 15(a)), the white asterisk (Figure 15(b)) and the orange bullet (Figure 15(c)). The inferred axes of the three jets identified in Figure 13(a) and (b) are denoted by the dashed blue arrow for the CJ and solid red arrows for SJ and SJ′. The position of the BBF near the surface is denoted by the cold front symbols. Tick marks are every 100 km. Note that the white area of cold OLR in the southeast half of the diagram is due to high cloud and that the drier air characterized by the dark shading extended beneath much of this region.

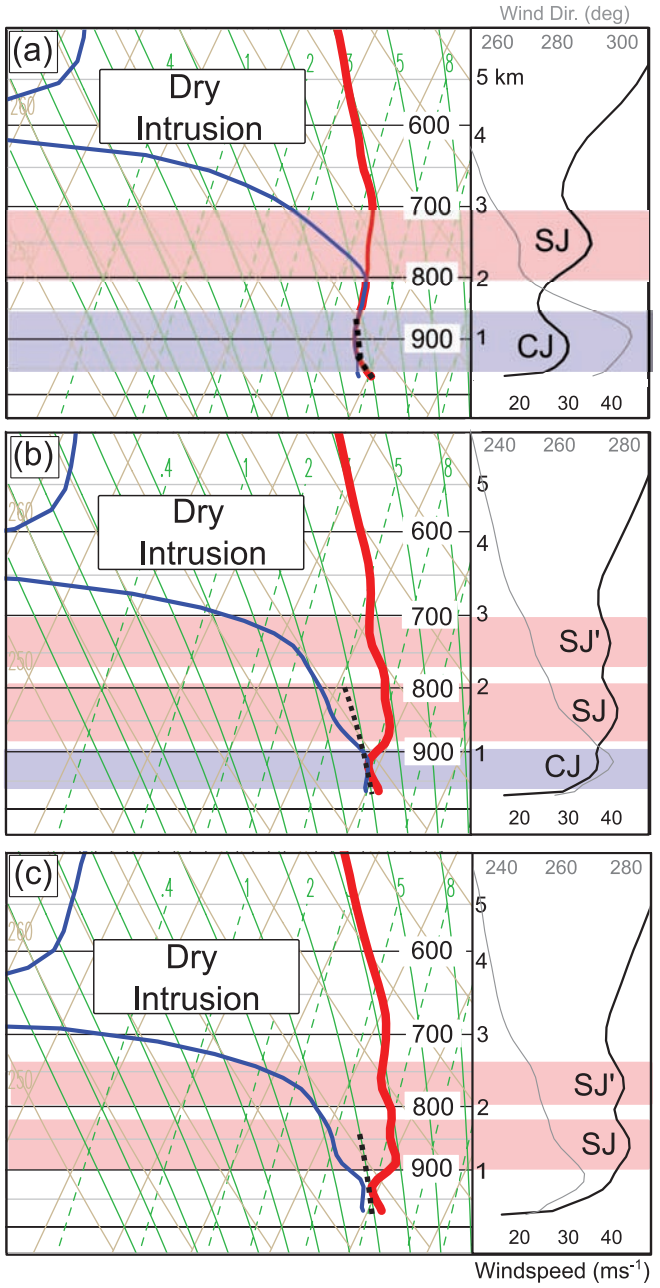


**Figure 15.** The structure of the LLJs in the lowest 5.5 km of the model domain at 0600 UTC on 28 October. Model soundings below 500 hPa: dry-bulb temperature (red curve) and dew-point temperature (blue curve) (left-hand panels) and horizontal wind speed (m s$^{-1}$) (bold, black curve) and wind direction (degrees from north, light grey curve) (right-hand panels), interpolated at (a) the blue bullet in Figure 14; (b) the location marked by the asterisk in Figure 14 and the dashed line (*) in Figure 13(a); and (c) the orange bullet in Figure 14. The vertical scale is given as pressure (hPa, left) and height (km, right). The paths of three hypothetical downdraught parcels, discussed in the text, are indicated by the bold, dashed lines. The approximate levels of the cores of SJ, SJ′ and CJ are indicated by the red and blue shading, respectively. The very dry air above the level of SJ and SJ′ is due to the descending dry intrusion.

situated within a boundary layer capped by a stable layer between 880 and 910 hPa. The 18 m s$^{-1}$ winds at the surface here are due to the CJ alone. The black dotted line shows the temperature of CJ air undergoing a vertical displacement within the boundary layer and indicates that the boundary layer in the model is marginally convectively unstable.

The sounding at the location of the asterisk, in Figure 15(b), is representative of the area of strong surface winds, observations of which were analyzed in the previous sections. Comparison with Doppler radar plots (e.g. Figure 12(b)) suggests that the observed LLJ analyzed in section 5 corresponds to the 40 m s$^{-1}$ sting jet labelled SJ in Figure 15(b), albeit with the observed jet being at a slightly lower level. (As noted above, there was also observational evidence of the higher-altitude SJ′, but this had less relevance than SJ to what was observed at the surface, at least in this region.) The observations revealed shallow elevated convection within SJ and indicated a role for downdraughts from these showers in bringing down high momentum to the surface. The dotted line in Figure 15(b) shows a trajectory for an air parcel able to descend with negative buoyancy from the top of the SJ all the way to the surface within such a downdraught, assuming it to be maintained at 100% saturation by evaporation. The fact that, in reality, such parcels were significantly subsaturated during descent suggests shortcomings in the model. As discussed later, it appears that the model underestimated the intensity of the convection associated with the sting jet. Finally, a plot of Richardson Number for this location (not shown) suggests very low values of Ri in the lowest 300 m, commensurate with shearing instability helping any such downdraught air to be mixed down to the surface.

The red bullet in Figure 14 is situated ahead of the leading edge of the CJ and the sounding at this location, in Figure 15(c), shows the two sting jets, SJ and SJ′, above the stable layer capping the boundary layer, but there is no sign of the CJ beneath it because the leading edge of the CJ was upstream of this location. Strong surface winds were also observed at this location and they would have been due to SJ, which reached 44 m s$^{-1}$ at 830 hPa: the dotted line in Figure 15(c) represents a downdraught associated with elevated convection within SJ (with the same caveats regarding the model as discussed for Figure 15(b)).

The properties of air parcels along trajectories starting within the cores of the CJ and SJ (16 each) in cross-section AA′ are shown in Figure 16. We shall consider first the SJ trajectories. These show that, at the time of Figure 13 (i.e. $t = 0$ in Figure 16), the SJ parcels were descending. Over the course of 3 h they descended

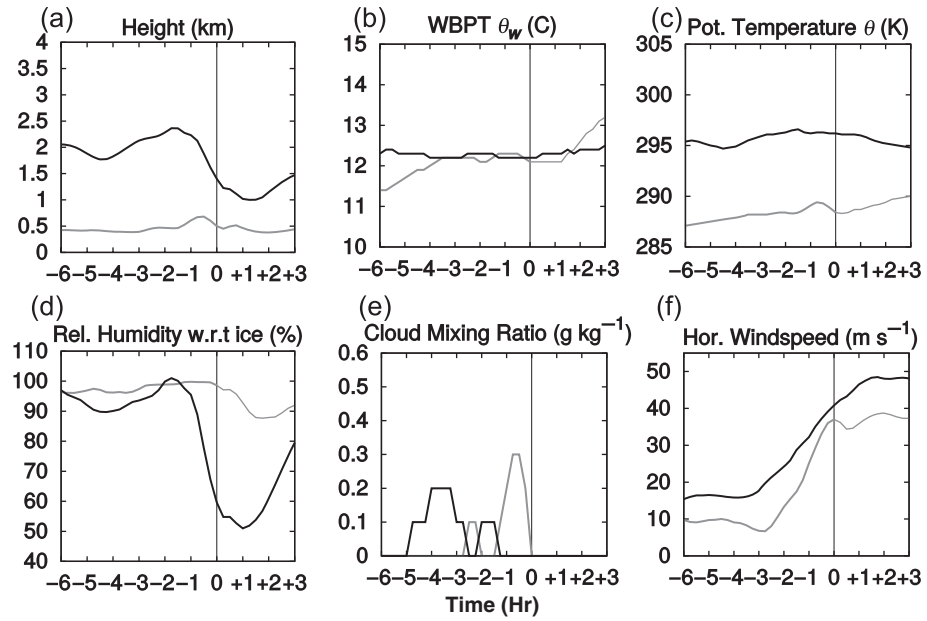


**Figure 16.** Trajectory diagnostics for the CJ and SJ parcels initialized at 0600 UTC on 28 October. Mean backward trajectories and forward trajectories based on a 4 × 4 array of 16 trajectories in the vertical plane, which were initialized at cross-section A–A′ within the boxes in Figure 13(a). (a) parcel height (km); (b) wet-bulb potential temperature, $\theta_w$ (C); (c) potential temperature, $\theta$ (K); (d) relative humidity w.r.t ice (%); (e) cloud mixing ratio (g kg$^{-1}$); (f) horizontal wind speed (ms$^{-1}$). CJ parcels are in grey and SJ parcels in black. Time is in model hours relative to the initialization time of the trajectories (0345 model time, 0600 real time).

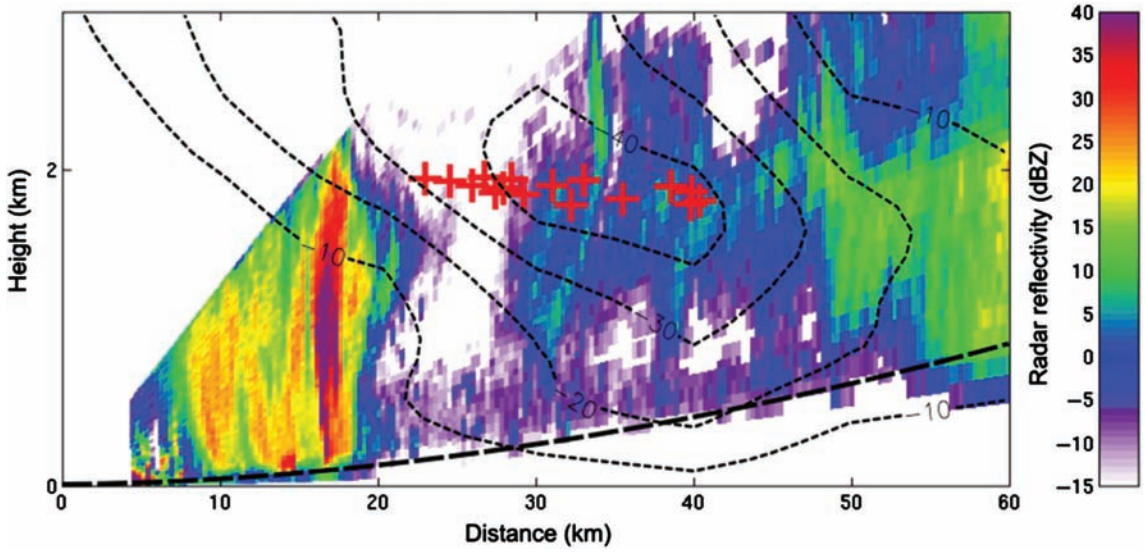


**Figure 17.** CAMRa RHI towards 260° (from north) at 0520 UTC on 28 October, showing showers in the region of the descending SJ trajectories about half an hour before most of the showers had evaporated entirely. Reflectivity (dBZ), shaded. The approximate radar horizon at 0.6° is shown by the dashed line. Vertical velocity contours every 10 cm s$^{-1}$ from −40 to −10 cm s$^{-1}$ (fine, short-dashed lines) from a comparable cross-section of the model run, adjusted for the time offset of the two sections, have been superimposed. Trajectories for SJ (red crosses) projected on the plane of the cross-section are shown (most trajectory parcels at this time lie within ±10 km of this plane).

about 1400 m (Figure 16(a)), during which time their wind speed doubled (Figure 16(f)). Cloud that had existed for several hours had evaporated by $t = -1$ h (Figure 16(e)) and relative humidity dropped from 100% to below 60% shortly afterwards (Figure 16(d)). The $\theta_w$ remained fairly constant, around 12.3 °C (Figure 16(b)), but the mean dry-bulb potential temperature of the sting-jet parcels decreased (Figure 16(c)), some individual parcels cooling by 2 °C or even more over a period of 2–3 h. However, the link between the time of the cooling and the time when the evaporation occurred in the SJ is not strong and so evidence, from the model alone, of the quantitative importance of evaporation is not clear.

The CJ also accelerated over the same period, reaching a speed of about 39 m s$^{-1}$ compared with 48 m s$^{-1}$ for SJ; however, it underwent less height change, remaining below 700 m throughout. The indication from the model that the sting jet was stronger than the CJ and that it occurred in a potentially unstable layer extending from the top of the boundary layer up to 2–3 km, where $\theta_w$ was comparable to that at the surface, is consistent with our earlier inference from the observations that convective showers were able to bring high momentum down through the CJ towards the surface within penetrative downdraughts. However, the intensity of the showers and convective instability, as well as the degree of evaporational cooling within the downdraughts, appeared to be significantly greater in reality than in the model.

What gives us confidence that we are at least qualitatively correct in suggesting a role for evaporational cooling is that the back-trajectories for the SJ parcels that are presented in Figure 16, having been initiated in a region where showers had largely dissipated (close to the location of the SJ label in Figure 12(a)), had previously passed through a region at 0520 where the observations showed abundant precipitation streamers (Figure 17). We note that Figure 16(e) shows that all of the model's cloud water had already evaporated in the region of the SJ trajectories by 0450; this is believed to be consistent with the model having underestimated the strength of the elevated convective instability of the resulting showers and the evaporational cooling.

## 7. Conclusions

A unique opportunity arose when a region of damaging winds from a rapidly deepening extratropical cyclone undergoing frontal fracture passed over the sensitive Doppler radar at Chilbolton in southern England. We have presented observational evidence from this radar and from a mesoanalysis of 1 min observations from the operational network of AWSs to show that convection and, most probably, evaporation played an important role in transferring momentum to the surface from a low-level jet that was located just above a shallow boundary layer. An observationally well-validated run from the WRF model confirmed that the LLJ was due to a sting jet, in which air parcels had descended within evaporating cloud filaments at the tip of the cyclone's cloud head, i.e. near the tip of the bent-back front. The observations and model showed that the strong surface wind gusts occurred where the surface temperature was beginning to fall and winds were veering in association with the arrival of a cold-conveyor-belt jet (CJ) that was situated in the boundary layer beneath the stronger sting jet. Momentum from the SJ was brought down through the CJ to the surface in places by convective circulations, accounting for some of the damaging winds.

We have identified three types of convection in the region of strongest winds.

(1) Narrow bands of convection orientated along the wind direction due to helical roll circulations entirely within the shallow boundary layer.
(2) Elevated convective cells up to 2 km deep within the SJ above the top of the boundary layer, associated with shafts of precipitation that were either evaporating or had recently evaporated.
(3) More widely spaced bands of convection orientated along the direction of the winds, due to penetrative convection in which momentum from the SJ was transferred to the surface in places.

We have inferred that evaporative cooling of air within the descending SJ was responsible for reducing[§] the static stability sufficiently for convective circulations to extend from the level of the SJ towards the surface. The inference was based on the following two findings. In one case, studied in particular detail, an ongoing but decaying shower was closely associated with a travelling patch of very strong surface gusts. The shower was observed to bring a column of high momentum down into the boundary layer, presumably as part of an evaporationally induced downdraught. In other places, the boundary-layer convection was observed to be engulfing high momentum from the SJ in places where the convective showers had largely decayed but are presumed to have left behind patches of cooler air aloft. The observational evidence for the role for evaporation is in one sense paradoxical, because the SJ momentum was observed to penetrate to the surface in regions where only vestiges of precipitation remained but, of course, this was simply due to the fact that the evaporation and associated cooling had been progressing for an hour or more by the time these events were occurring.

A way for forecasters to determine whether and where these processes might be occurring is to use satellite infrared imagery to identify a small dark zone (area of reduced cloud where the SJ air descends strongly) near the tip of a cloud-head filament (see also Smart and Browning, 2014, their section 4.2). Sometimes, as in the present case, this dark zone is in the shape of a chevron wrapped around the tip of the cloud filament. In the Great Storm of October 1987 and to a lesser extent in the present case, the leading edge of the dark chevron was marked by a chevron-shaped arc of shallow cloud which, according to Browning and Field (2004), may be associated with an arc of boundary-layer convergence just ahead of where the divergent sting-jet air has penetrated to the surface. The issue of how the model represents the types of boundary-layer circulation, convective showers, evaporation and momentum transfer at medium and high resolution requires further investigation.

[§]Compared with what the static stability would have been in the presence of unmitigated adiabatic warming of the descending SJ.

## Acknowledgements

We thank Chris Westbrook (University of Reading) and Chris Walden (Rutherford Appleton Laboratory) for help with the radar data analysis and Darcy Ladd (Chilbolton Observatory), who helped with operating the radar on the night of the storm. The Chilbolton Facility for Atmospheric and Radio Research (CFARR) is managed on behalf of the National Environment Research Council (NERC) by the National Centre for Atmospheric Science (NCAS) and operated by the Science and Technology Facilities Council. Additional observations were made possible as part of the Met Office High Impact and Extreme Weather Experiment (HIEWEX). KAB and DJS thank Professors Julian Hunt (UCL), Michael Manton (University of Monash) and David Schultz (University of Manchester) for discussions and comments regarding a previous version of the article. Two anonymous referees are thanked for detailed and thoughtful comments, which led to substantial improvements in the manuscript. The contribution of MRC is Crown copyright UKMO.

## References

Baker LH, Gray SL, Clark PA. 2014. Idealised simulations of sting-jet cyclones. *Q. J. R. Meteorol. Soc.* **140**: 96–110, doi: 10.1002/qj.2131.

Browning KA. 2004. The sting at the end of the tail: Damaging winds associated with extra-tropical cyclones. *Q. J. R. Meteorol. Soc.* **130**: 375–399, doi: 10.1256/qj.02.143.

Browning KA, Field M. 2004. Evidence from Meteosat imagery of the interaction of sting jets with the boundary layer. *Meteorol. Appl.* **11**: 277–289, doi: 10.1017/S1350482704001379.

Browning KA, Hill FF. 1984. Structure and evolution of a mesoscale convective system near the British Isles. *Q. J. R. Meteorol. Soc.* **110**: 897–913.

Clark MR, Parker DJ. 2014. On the mesoscale structure of surface wind and pressure fields near tornadic and nontornadic cold fronts. *Mon. Weather Rev.* **142**: 3560–3585.

Clark PA, Browning KA, Wang C. 2005. The sting at the end of the tail: Model diagnostics of fine-scale three-dimensional structure of the cloud head. *Q. J. R. Meteorol. Soc.* **131**: 2263–2292, doi: 10.1256/qj.04.36.

Fujita TT. 1955. Results of detailed synoptic studies of squall lines. *Tellus* **7**: 405–436.

Fujita TT. 1958. Mesoanalysis of the Illinois tornadoes of 9 April 1953. *J. Meteorol.* **15**: 288–296.

Goddard FW, Eastment JD, Thurai M. 1994. The Chilbolton advanced meteorological radar: A tool for multidisciplinary atmospheric research. *Electron. Commun. Eng. J.* **6**: 77–86.

Gray SL, Martinez-Alvarado O, Baker LH, Clark PA. 2011. Conditional symmetric instability in sting-jet storms. *Q. J. R. Meteorol. Soc.* **137**: 1482–1500, doi: 10.1002/qj.859.

Koch SE, O'Handley C. 1997. Operational forecasting and detection of mesoscale gravity waves. *Weather and Forecasting* **12**: 253–281.

Kosiba KA, Wurman J. 2014. Finescale dual-Doppler analysis of hurricane boundary layer structures in Hurricane Frances (2004) at landfall. *Mon. Weather Rev.* **142**: 1874–1891, doi: 10.1175/MWR-D-13-00178.1.

Li L, Kareem A, Hunt J, Xiao Y, Zhou C, Song L. 2015. Turbulence spectra for boundary-layer winds in tropical cyclones: A conceptual framework and field measurements at coastlines. *Boundary-Layer Meteorol.* **154**: 243–263, doi: 10.1007/s10546-014-9974-7.

Martinez-Alvarado O, Weidle F, Gray SL. 2010. Sting jets in simulations of a real cyclone by two mesoscale models. *Mon. Weather Rev.* **138**: 4054–4075, doi: 10.1175/2010MWR3290.1.

Martinez-Alvarado O, Gray SL, Catto JL, Clark PA. 2012. Sting jets in intense winter North-Atlantic windstorms. *Env. Res. Lett.* **7**: 024014, doi: 10.1088/1748-9326/7/2/024014.

Martinez-Alvarado O, Baker LH, Gray SL, Methven J, Plant RS. 2014. Distinguishing the cold conveyor belt and sting jet airstreams in an intense extratropical cyclone. *Mon. Weather Rev.* **142**: 2571–2595, doi: 10.1175/MWR-D-13-00348.1.

Nakanishi M, Niino H. 2004. An improved Mellor–Yamada level 3 model with condensation physics: Its design and verification. *Boundary-Layer Meteorol.* **112**: 1–31, doi: 10.1023/B:BOUN.0000020164.04146.98.

Olson JB, Brown JM. 2012. 'Modifications to the MYNN PBL and surface layer scheme for WRF-ARW'. In *13th Annual WRF Users' Workshop, Paper 3.3*, Boulder, CO.

Parton GA, Vaughan G, Norton EG, Browning KA, Clark PA. 2009. Wind profiler observations of a sting jet. *Q. J. R. Meteorol. Soc.* **135**: 663–680, doi: 10.1002/qj.398.

Schultz DM, Sienkiewicz JM. 2013. Using frontogenesis to identify sting jets in extratropical cyclones. *Mon. Weather Rev.* **28**: 603–613, doi: 10.1175/WAF-D-12-00126.1.

Shapiro MA, Keyser D. 1990. Fronts, jet streams and the tropopause. In *Extratropical Cyclones: The Erik Palmén Memorial Volume*, Newton CW, Holopainen EO. (eds.): 167–191. American Meteorological Society: Boston.

Skamarock WC, Klemp JB, Dudhia J, Gill DO, Barker DM, Duda MG, Huang X-Y, Wang W, Powers JG. 2008. 'A description of the Advanced Research WRF Version 3', NCAR Technical Note NCAR/TN-475+STR, Boulder, CO.

Slater TP, Schultz DM, Vaughan G. 2014. Acceleration of near-surface strong winds in a dry, idealised extratropical cyclone. *Q. J. R. Meteorol. Soc.* **141**: 1004–1016, doi: 10.1002/qj.2417.

Smart DJ, Browning KA. 2014. Attribution of strong winds to a cold conveyor belt and sting jet. *Q. J. R. Meteorol. Soc.* **140**: 595–610, doi: 10.1002/qj.2162.